nature materials

ARTICLES

https://doi.org/10.1038/s41563-018-0252-9

Observation of higher-order topological acoustic states protected by generalized chiral symmetry

Xiang Ni[1,2], Matthew Weiner[1,2], Andrea Alù[1,2,3*] and Alexander B. Khanikaev[1,2*]

Topological systems are inherently robust to disorder and continuous perturbations, resulting in dissipation-free edge transport of electrons in quantum solids, or reflectionless guiding of photons and phonons in classical wave systems characterized by topological invariants. Recently, a new class of topological materials characterized by bulk polarization has been introduced, and was shown to host higher-order topological corner states. Here, we demonstrate theoretically and experimentally that 3D-printed two-dimensional acoustic meta-structures can possess nontrivial bulk topological polarization and host one-dimensional edge and Wannier-type second-order zero-dimensional corner states with unique acoustic properties. We observe second-order topological states protected by a generalized chiral symmetry of the meta-structure, which are localized at the corners and are pinned to 'zero energy'. Interestingly, unlike the 'zero energy' states protected by conventional chiral symmetry, the generalized chiral symmetry of our three-atom sublattice enables their spectral overlap with the continuum of bulk states without leakage. Our findings offer possibilities for advanced control of the propagation and manipulation of sound, including within the radiative continuum.

Topological phases of matter support some of the most fascinating properties for signal transport and wave propagation, holding the promise of revolutionizing technologies from quantum electronics[1–7] to photonics[8–25] and acoustics[26–30]. In electronics and quantum photonics, they have been opening novel approaches for quantum computing interfaces[31,32] and lasing[33–35], while in classical optics, mechanical and acoustic systems, they offer unprecedented robustness to defects and disorder[10–20,22,24,26–29,36]. Most of the topological systems studied so far are characterized by topological indexes, such as Chern-class numbers, $Z2$ invariants and winding numbers. More recently, a new class of symmetry-protected topological phases, characterized by bulk polarization, has been introduced theoretically[37]. One example of such systems is given by quadrupole topological insulators[38,39], which have been recently implemented in mechanical[40] and microwave[41] systems, as well as in electrical circuits[42]. However, higher-order topological insulators are not limited to the category of quadrupole topological insulators, and our two-dimensional system exhibits 'zero-energy' states localized at the corners, with gapped bulk and edge bands, and topological invariants characterized by bulk polarization. All these features meet the definition of a higher-order topological insulator[43–50] and, more specifically, of a Wannier-type second-order topological insulator. A criterion to distinguish topological corner states from trivial ones is that they are protected by time reversal or spatial symmetries[51]. In our system, the corner states are pinned to 'zero energy' and localize at one of the sublattices—a property attributed to the conservation of the generalized chiral symmetry introduced here for the system with three sublattices.

The class of topological systems with zero Berry curvature but nontrivial bulk polarization offers an opportunity to implement robust, controllable physical responses. Here, we theoretically analyse and experimentally demonstrate the confinement of higher-order corner states and their inherent robustness by deliberately introducing disorder. In addition, these corner states are transformed into embedded eigenstates within the continuum of bulk modes by tuning the hopping parameters without changing the bulk polarization and breaking the generalized chiral symmetry. These findings open opportunities for acoustic and photonic devices based on topological bulk polarization and topological embedded corner eigenstates.

Acoustic metamaterial design

We explore a two-dimensional acoustic kagome lattice[44,52] characterized by bulk polarization (Supplementary Sections 2,3), supporting a topological phase protected by lattice symmetries. The lattice is shown schematically in Fig. 1a and is formed by an array of acoustic resonator trimers coupled via narrow rectangular channels (Fig. 1b, c). Each resonator hosts acoustic pressure modes oscillating in the axial direction. We choose to work with the fundamental mode (~4.23 kHz), which has its only node at the centre of the resonant cavity. The coupling strength is tuned by shifting the channels closer to or farther away from the centre node, thus enabling fine control over the local coupling strength, which is demonstrated experimentally by the frequency responses of single trimer in Supplementary Section 4. Due to the strong confinement of the resonant modes and the connectivity of the lattice, the system is approximated well by the tight-binding model (TBM) (Supplementary Section 1) except in the case when there is an open boundary condition (Supplementary Section 11), with nearest-neighbour coupling described by intercell γ and intra-cell κ coupling parameters (Fig. 1a). For the case of an ideal kagome lattice, with $\gamma = \kappa$, the band diagram obtained with TBM (grey solid lines in Fig. 1d) supports a Dirac-like degeneracy at the K and K′ points. The degeneracy is formed between low-frequency monopolar modes, characterized by in-phase vibrations in all three cylinders of the trimer, and dipolar modes, which are left- and right-hand circularly polarized at the K and K′ points, respectively.

[1]Department of Electrical Engineering, Grove School of Engineering, City College of the City University of New York, New York, NY, USA. [2]Physics Program, Graduate Center of the City University of New York, New York, NY, USA. [3]Photonics Initiative, Advanced Science Research Center, City University of New York, New York, NY, USA. *e-mail: aalu@gc.cuny.edu; akhanikaev@ccny.cuny.edu

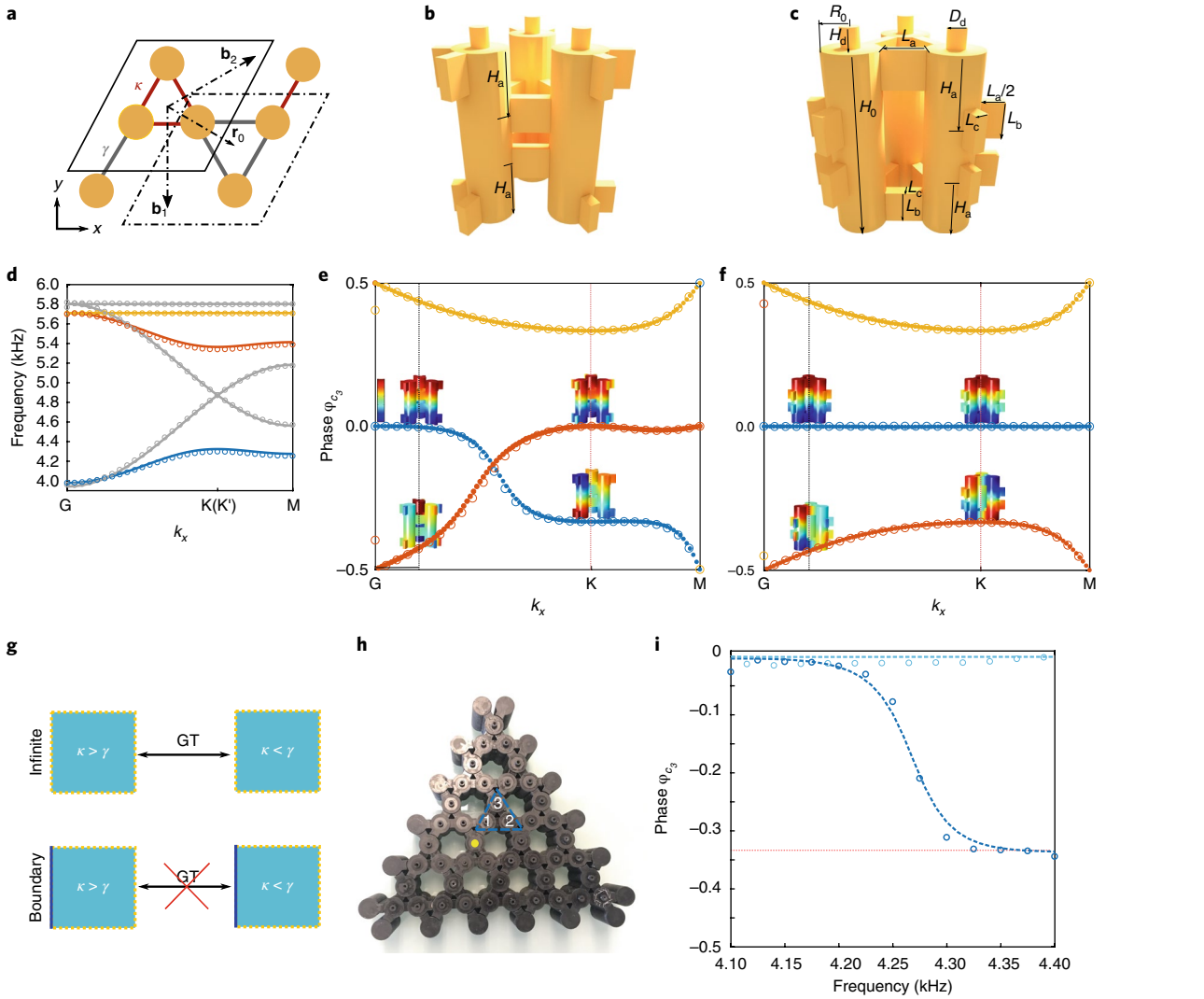

Fig. 1 | Concept and measurement of the bulk polarization transition in the deformed kagome lattice. a, Schematics of the 2D tight-binding kagome lattice. **b**,**c**, Realistic acoustic trimer for 'expanded' (**b**) and 'shrunken' (**c**) lattice designs, which emulate the effect of nearest-neighbour coupling. **d**, Band structures of the kagome lattice obtained by TBM (solid lines) and first-principles calculation (circular dots), separately. Grey lines are the band structures of the undeformed kagome lattice, and blue, red and yellow lines are the band structures of expanded/shrunken kagome lattice. **e**,**f**, ϕ_{C_3} normalized to 2π, along the high-symmetry point lines of the expanded (**e**) and shrunken (**f**) lattice. Blue, red and yellow lines represent the phases ϕ_{C_3} of the bands with corresponding colours in **d**. The inset colour map describes the acoustic pressure of the sketched structures. **g**, Schematic relationships between the eigenstates of the expanded lattice and the shrunken lattice without a boundary (top) and with a boundary (bottom). GT represents that the relation between two eigenstates is gauge tranformative. **h**, Photograph of the printed acoustic lattice. The array consists of five cells at each edge, with boundary cells that have a higher resonance frequency to terminate the array. These boundary cells play a crucial role in emulating the open boundary condition in TBM (Supplementary Section 11). A speaker is placed at the yellow spot and phase measurements are taken in the triangular region marked by blue lines. **i**, ϕ_{C_3} of the lowest bulk band for topological nontrivial (dark blue) and trivial geometries (light blue). Both theoretical and experimental results are shown, denoted by dashed line and circle-shaped markers, respectively. The red dashed line indicates the position of $-1/3$.

We stress that the geometry of Fig. 1 can be viewed as the two-dimensonal counterpart of the well-known one-dimensional Su–Schrieffer–Heeger (SSH) model. As the symmetry is reduced by detuning inter-cell γ and intra-cell κ couplings between neighbouring trimers, a topological transition emerges in the band diagram. Specifically, the trimers in Fig. 1b, c (geometry provided in the section 'Structure design, 3D printing and generic measurements' in Methods) support bandgaps at both K and K′ valleys with topologically nontrivial ($\gamma > \kappa$) and trivial ($\gamma < \kappa$) nature (referred to as expanded and shrunken, respectively), implying that a control over the coupling parameters can enable ad hoc topological transitions. The symmetry reduction from six-fold rotational symmetry (C_6) to three-fold rotational symmetry (C_3) leads to hybridization and avoided crossing of formerly degenerate dipolar and monopolar bands, giving rise to the band inversion. The cases of equal detuning for $\gamma > \kappa$ and $\gamma < \kappa$ have identical band structure, shown in Fig. 1d by solid lines, and therefore cannot be distinguished. However, these two cases represent two distinct topological phases, separated by the gapless $\gamma = \kappa$ transition point. The topological transition is demonstrated by directly calculating the bulk polarization (see Supplementary Fig. 1) through a Wilson loop, and also by investigating the C_3-related properties at high-symmetry points in the Brillouin zone for the case of ideal symmetries, as we discuss in the following. In addition to the results from the TBM, the circular markers plotted in Fig. 1d illustrate first-principles simulations obtained by directly solving the three-dimensional pressure-wave

equation using the finite element method (FEM). The accurate agreement between analytical and numerical results serves as further evidence of the applicability of the TBM and the related theoretical analysis (simulation details and fitting parameters can be seen in the section 'Numerical methods' in Methods).

The bulk polarization characterizes the displacement of the average position of Wannier states from the sites' centre of the unit cell[39,50]. In the trivial case, the zero value of bulk polarization indicates modes that are pinned to the sites' centre, and no modes hang at the boundaries. However, in the topological nontrivial case, the bulk polarization is nonzero, inducing modes at the boundaries away from the bulk, and causing localization at the dangling sites of the boundary. Additionally, we have developed the theory of polarization difference to characterize the distinction between shrunken and expanded unit cells, which is detailed in Supplementary Section 5. The shrunken and expanded unit cells, with their hopping κ and γ swapped, can be transformed into each other by a series of uniform transformations when the lattice is infinitely large; thus their eigenstates are connected through the gauge transformation. The nontrivial polarization difference manifests in topological effects only when there is a boundary in the lattice. The presence of a boundary breaks the gauge transformation and makes it impossible to connect the eigenstates of the two systems (Fig. 1g), giving rise to boundary effects in the form of topological edge and corner states when the bulk polarization is nontrivial. Thus, as we show here, the bulk polarization difference of the three-fold symmetric kagome lattice acquires the values $(1/3, 1/3)$ upon the spatial translation (by a vector $\mathbf{r}$, as shown in Fig. 1a) and the subsequent rotation substituting shrunken and expanded unit cells, and leads to the emergence of edge and corner states at the boundaries of the expanded lattice.

Bulk polarization measurement. To confirm the topological transition as we tune the coupling going from the expanded to the shrunken lattice, we extract the bulk polarization using both the TBM and FEM in a visual way, so that the information about the irreducible representation of symmetry groups is revealed in momentum space. As shown in Supplementary Section 3, the polarization is directly related to the constraints imposed by the symmetry operations on the eigenvectors. In particular, following the work of Fang et al.[37], when C_3 symmetry is preserved we can extract the polarization directly from the eigenvalue of C_3 symmetry, as detailed in Supplementary Section 6. The bulk polarization assumes the form

$$\mathrm{e}^{-i\pi(p_i)} = \prod\nolimits_{n\in\mathrm{occ}} \frac{\theta_n(\mathrm{K})}{\theta_n(\Gamma)} \tag{1}$$

where $\theta_n(\mathbf{k}) = \langle u_n(\mathbf{k})|R_3|u_n(\mathbf{k})\rangle$ is the expectation value of the three-fold symmetric operator R_3 (rotation by $2\pi/3$) applied to eigenvector $u_n(\mathbf{k})$. The index i represents the reciprocal vector $\mathbf{b}_i$ in the Brillouin zone (Fig. 1a); correspondingly, p_i is the bulk polarization in this direction. Because of the conservation of C_3 symmetry, p_i is identical in different directions. The subscript 'occ' in equation (1) implies the summation over the bands below the bandgap of interest (as opposed to the occupied bands below the Fermi level in the condensed matter). We define the following quantity

$$\phi_{C_3}(\mathbf{k}) = -i\log(\theta_n(\mathbf{k})) \tag{2}$$

which is essential in observing the dependence of the eigenstates' rotational symmetry on the momentum vector $\mathbf{k}$. This quantity, plotted in Fig. 1e, f, clearly reveals the difference between expanded ($\gamma > \kappa$) and shrunken ($\gamma < \kappa$) cases. This approach allows a straightforward physical interpretation of topological phase: in the topological nontrivial regime, the action of the R_3 operator on the eigenstate of the lowest band at the K (or K′) point yields the eigenvalue $2\pi/3$, associated with the rotational dipolar field-profile (blue line in Fig. 1e). In the topologically trivial regime, the mode pattern is not rotating in the entire Brillouin zone, giving rise to no phase difference between K and Γ points (blue line in Fig. 1f).

Interestingly, this approach enables an alternative way of accurately extracting the bulk polarization by evaluating $\phi_{C_3}(\mathbf{k})$ only at C_3-invariant points of the Brillouin zone. The bulk polarization of the band of interest can therefore be defined as the difference of $\phi_{C_3}(\mathbf{k})$ at different C_3-invariant points, K and Γ points, respectively—that is, $p_i = \phi_{C_3}(\Gamma) - \phi_{C_3}(\mathrm{K})$ for the lowest band of interest. For the lower-frequency (blue-coloured) band, the bulk polarizations can be readily seen from Fig. 1e, f as

$$(p_1, p_2) = \begin{cases} (-1/3, -1/3), & \kappa < \gamma \\ (0, 0), & \kappa > \gamma \end{cases} \tag{3}$$

which clearly indicate distinct topologically nontrivial and trivial phases, respectively.

To extract experimentally the bulk polarization in a finite acoustic meta-structure, we exploit the bijective relations between frequency, momentum vector, and phase $\phi_{C_3}(\mathbf{k})$ of the bulk mode, which is valid for an isolated low-frequency band at C_3-invariant points. These relations hold true due to the fact that the corresponding bulk band has the lowest frequency at the Γ point, and the highest frequency at the K(K′) point. In addition, the relative direction connecting source (speaker) and detector (microphone) can be selected so that modes with either positive or negative (relative to the positive direction) momentum vectors are probed. Therefore, the mode at the Γ point can be probed by a low-frequency excitation, whereas the modes at the K(K′) point can be probed by driving the system with high frequencies (close to the lower-frequency edge of the topological bandgap).

The acoustic kagome lattices of Fig. 1 were fabricated using a B9Creations stereolithographic 3D printer (see the section 'Structure design, 3D printing and generic measurements' in Methods). As shown in Fig. 1h, the source was placed at the centre of the structure (indicated by the yellow dot) and two detectors were placed inside blue trimers of either topological nontrivial or trivial lattices. The relative direction between source and detectors corresponds to the case of excitation with either positive or negative momentum. Thus, by sweeping the frequency of the source over the desired spectral range, we measured the field profiles of the excited bulk mode and obtained the phase differences of the three sites within the trimer (for example, φ_{12} and φ_{13}). Then we constructed the normalized eigenstate of the mode as $1/\sqrt{3}\,(1, \mathrm{e}^{i\varphi_{12}}, \mathrm{e}^{i\varphi_{13}})$, and extracted the phase ϕ_{C_3} based on this constructed eigenstate. Details of phase measurement, data acquisition and data processing are described in the section 'Phase difference measurement' in Methods. As shown in Fig. 1i, the measurement results (circular markers) and first-principles simulations (dashed lines) clearly show that the phase ϕ_{C_3} sweeps 1/3 of 2π for the case of the topological lattice and remains at 0 for the topologically trivial lattice. These results unambiguously confirm and experimentally verify the topological polarization of 1/3 of the corresponding low-frequency bulk band for the expanded lattice. We also measured the phase differences and extracted the phase ϕ_{C_3} of the topological case in the expanded and shrunken lattices, respectively (Supplementary Section 7). These results confirm the essential features of nontrivial bulk polarization difference, namely, the eigenstates of infinite expanded and shrunken lattices are gauge transformative.

Zero-energy corner states protected by Γ_3 symmetry

A prominent distinction between topological and trivial phases of matter consists in the robust emergence of topological edge states

exponentially confined to the boundaries[52]. As seen from the blue region of Fig. 2a, the triangular kagome lattice in the topological regime supports topological edge states, which emerge from the non-vanishing bulk polarization (the proof is detailed in Supplementary Section 8a), in contrast to the edge states due to nontrivial Berry curvature in quantum spin Hall effect and valley Hall effect systems.

In addition to the edge states, the energy spectrum (red line in Fig. 2a) suggests another class of totally dispersionless states with their analytic solutions obtained in Supplementary Section 8b, and their field profile reveals their zero-dimensional nature. These states indeed represent a class of higher-order (D-2) topological states, which are confined to corners of the system when the angle of the corner equals 60° and only one of the sublattice sites is located at the corner (the proof can be found in Supplementary Section 9). For all values of parameter $\kappa < \gamma$ (with fixed γ), these states are pinned to 'zero-energy', which, for this acoustic system, represents the frequency of the isolated acoustic resonator. The 'zero-energy' corner modes we observe are protected by the generalized chiral symmetry Γ_3 specific for the structure with three sublattices. The generalized chiral symmetry Γ_3 transforms Hamiltonian H_0 in the following way, if H_0 respects this symmetry,

$$\begin{aligned} \Gamma_3 H_0 \Gamma_3^{-1} &= H_1 \\ \Gamma_3 H_1 \Gamma_3^{-1} &= H_2 \end{aligned}$$

$$H_0 + H_1 + H_2 = 0 \tag{4}$$

where H_1 and H_2 are isomorphic to H_0. Based on the definitions in equation (4), we prove the following: if the chiral symmetry Γ_3 is preserved, the sum of the three eigenenergies of H_0 is zero; if the triple degenerate zero-energy states exist, these states localize only at one of the sublattices. The comprehensive proofs of these statements and other properties related to generalized chiral symmetry operators Γ_3 are detailed in Supplementary Section 10. Using these properties of operator Γ_3, we can judge whether the system possesses the generalized chiral symmetry and the corner states appear due to the conservation of this symmetry.

We emphasize that the edge state in one-dimensional SSH modes, as well as midgap corner modes reported recently in the work of Noh et al.[53], are protected by chiral symmetry due to the presence of two sublattices, which ensures that the states $\epsilon_{0D} = 0$ always appear in the centre of the bulk gap between $\epsilon_1 = -\epsilon_{bulk}(\mathbf{k})$ and $\epsilon_2 = \epsilon_{bulk}(\mathbf{k})$ bands. In our case, however, because the generalized chiral symmetry implies $\epsilon_1 + \epsilon_2 + \epsilon_3 = 0$, the zero-energy corner state $\epsilon_{0D} = 0$ may appear not only in the bandgap but also can coexist with the bulk continuum.

Apart from their nontrivial bulk polarization, the corner states protected by Γ_3 symmetry exist in two distinct regimes. In the first regime, when the symmetry reduction is large, and $\kappa/\gamma < 0.5$, these states are embedded in the bandgap induced by the topological transition (white region on the right side of Fig. 2a). In the second regime, when $1 > \kappa/\gamma > 0.5$, symmetry reduction due to the expansion effect is not sufficient to lift a bulk gap wide enough and, as a result, the corner states pinned to 'zero energy' are embedded in the bulk continuum, becoming embedded eigenstates[54–58]. Our numerical calculations of the supercell demonstrate that these 0D topological eigenstates do not interact with bulk states, despite being compatible with radiation in the bulk in terms of momentum, and multiple degeneracies (crossings) between bulk and corner spectra are observed. In all regimes, the corner states exhibit an exponential decay with plane-wave-like modulation in the direction bisecting the corner.

When the ratio κ/γ is equal to 0.252, as shown by the blue dashed line in Fig. 2a, bulk, edge and corner modes are well separated from each other. To verify the localization of edge states and corner states, the spatially resolved eigenstate distributions $|\psi(\omega)|^2$ integrated over the corresponding frequencies (indexed by I to IV) are plotted in Fig. 2b. To reveal all the states hosted by both the topological and trivial structures, we measured the local density of states, as shown in Fig. 2c, d, respectively (refer to the section 'Density of states measurement' in Methods for details). The density of states was extracted by studying the local response through exciting and probing pressure fields at the same location at each lattice site. The measurement was performed over a broad frequency range that enclosed both low- and high-frequency bulk bands. In agreement with the results in Fig. 2b, the measured field profiles corresponding to the excitation of the low-frequency bulk, edge, corner and high-frequency bulk states of the expanded lattice (Fig. 2e) clearly highlight the different nature of the different bands (for comparison, the measured field profiles of the shrunken lattice are presented in Supplementary Fig. 9). As expected, the spatially resolved power distribution integrated over the respective frequency ranges is directly related to the peaks in the measured density of states distribution in Fig. 2c, and the spatial power distributions in Fig. 2e panels II and III correspond to the excitation of edge (blue shaded region) and corner (red shaded region) states, which arise only in the topological lattice. As seen from the field profiles of the corner states in Fig. 2e panel III, only one of the three sublattice sites at each corner is excited, which is due to the conservation of the generalized chiral symmetry.

The observed small overlap of the corner states with upper bulk modes is explained as the result of inhomogeneous broadening caused by the finite lifetime of the modes in the experimental set-up. We found that the main mechanisms contributing to the broadening were the geometrical deviations due to limited fabrication precision, as well as radiative loss through the probe (excitation) channels. Nonetheless, as seen from the comparison with the theoretical data shown in red circles on the horizontal axis of Fig. 2c, d, the experimental data are in very good agreement with first-principles results, indicating that neither factor affects the topological nature of the modes, confirming their robustness, or alters their spectral position.

Robustness of the corner states

The strong localization of the corner state in one of the sublattices due to Γ_3 symmetry implies that that this state should be insensitive against disorder in other sublattices. To confirm this property, we selected again the case when $\kappa/\gamma = 0.252$ and performed TBM studies of disordered systems with the cylinders inside the yellow dashed regions (Fig. 3b) having their resonant frequencies randomly distributed around the frequency of the corner cylinder. In this case, the generalized chiral symmetry is globally preserved because the feature of Γ_3-symmetry-protected corner states is unchanged, although the local generalized chiral symmetry at the corners is broken. As predicted, we found that the corner state remains pinned to the same frequency (Fig. 3a). On the other hand, the frequency of the corner state is sensitive to the perturbation of the resonator heights it was pinned to. In this case, the frequency of the corner state deviates from 'zero energy' as the degree of perturbation increases (Fig. 3d). Such insensitivity to the disorder of sublattice corner states not pinned to, suggests possible applications for sensing where the mode can be well confined.

We experimentally investigated the robustness properties of the corner states. As suggested by theoretical results, these modes should exhibit robustness against disorder as long as the sublattice sites of the corner states are unperturbed. To test this, we fabricated several trimers (yellow dashed regions in Fig. 3b) with deliberately introduced random deviations of up to 10% in their height,

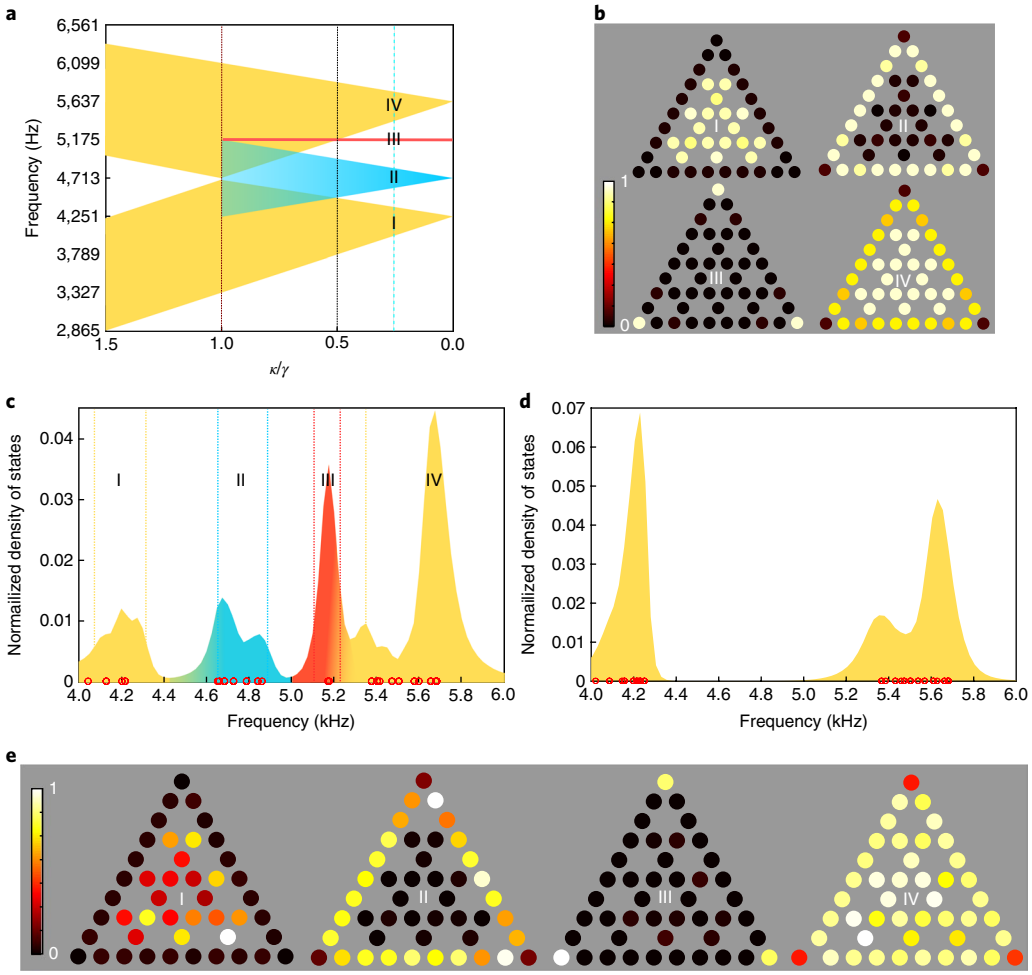

Fig. 2 | Theoretical prediction and experimental demonstration of acoustic edge and corner states. a, Energy spectrum calculated from TBM for the triangular kagome lattice. Yellow, blue and red bands are for bulk, edge and corner states, respectively. **b**, Normalized spatial distribution of $|\psi(\omega)|^2$ integrated over the frequencies of lower bulk, edge, corner and upper bulk regions, respectively, where $\kappa/\gamma = 0.252$ is denoted by blue dashed line in **a**. $\psi(\omega)$ is the eigenstate of the triangular kagome lattice. **c**, Normalized density of states for the expanded lattice obtained from the measurements of acoustic power at the top of the trimer. Red, blue and yellow regions are colour-coded to represent corner, edge and bulk modes dominating in these regions. Red, blue and yellow dashed vertical lines show the lower and upper bounds of the integrations used in **e**. **d**, Normalized density of states for the shrunken lattice obtained from the acoustic power measured at the top of the trimer. Results from numerical calculations are marked in red circles in both **c** and **d**. **e**, Spatial distributions of the acoustic power integrated over the respective frequency regions indexed by Roman numerals (from I to IV).

and placed them next to the corner trimer, in which all sites except sublattice sites of the corner states were randomly perturbed to the same degree. As a result of the perturbation introduced, the resonant frequency of the individual cylinders next to the corner fluctuated randomly by up to 400 Hz, which is about 40% of the spectral width of the topological bandgap. The acoustic pressure field distribution integrated over the corner spectral range (Fig. 3b) confirms that the corner states retain their strong confinement, and do not leak into either the bulk or edge states. The measured density of states confirms that the corner states remain well defined and pinned to 'zero energy' in the spectrum, and overlap with the corner states for the unperturbed lattice, indicating their robustness against disorder in adjacent sublattices (Fig. 3c).

In a second measurement, the three corner trimers of the printed structure were perturbed by a deviation of up to 10% in their height (yellow dashed region in Fig. 3e), except at the corner site, which was left unperturbed. We found that the corner states no longer localized at one of the sublattices, and spurious modes are present and dominate over these corner modes, as can be seen from the spatially resolved power distribution integrated over the frequency range of the corner states Fig. 3e. The mismatch of corner states spectra between the perturbed and unperturbed lattices confirms the prediction that these corner states are no longer protected by the generalized chiral symmetry and are not pinned to 'zero energy'.

Topological corner states embedded in the continuum

Next, we studied the case of corner states embedded in the continuum of bulk states, a unique feature enabled by the presence of the three sublattices and the generalized chiral symmetry, which ensures that $\epsilon_1+\epsilon_2+\epsilon_3=0$, for bulk modes (as opposed to $\epsilon_1+\epsilon_2=0$ for the conventional chiral symmetry of a bipartite lattice), while the corner state remains pinned to 'zero energy'. To this aim, we fabricated another topological sample with detuning between inter-cell and intra-cell channels such that the corner states would spectrally overlap with high-frequency bulk modes, corresponding to the ratio $\kappa/\gamma=0.52$ in Fig. 2a. The corner states were probed by placing a source at the three corner sites of the topological structure, which were driven at 5,250 Hz. Bulk states at such a frequency are mostly

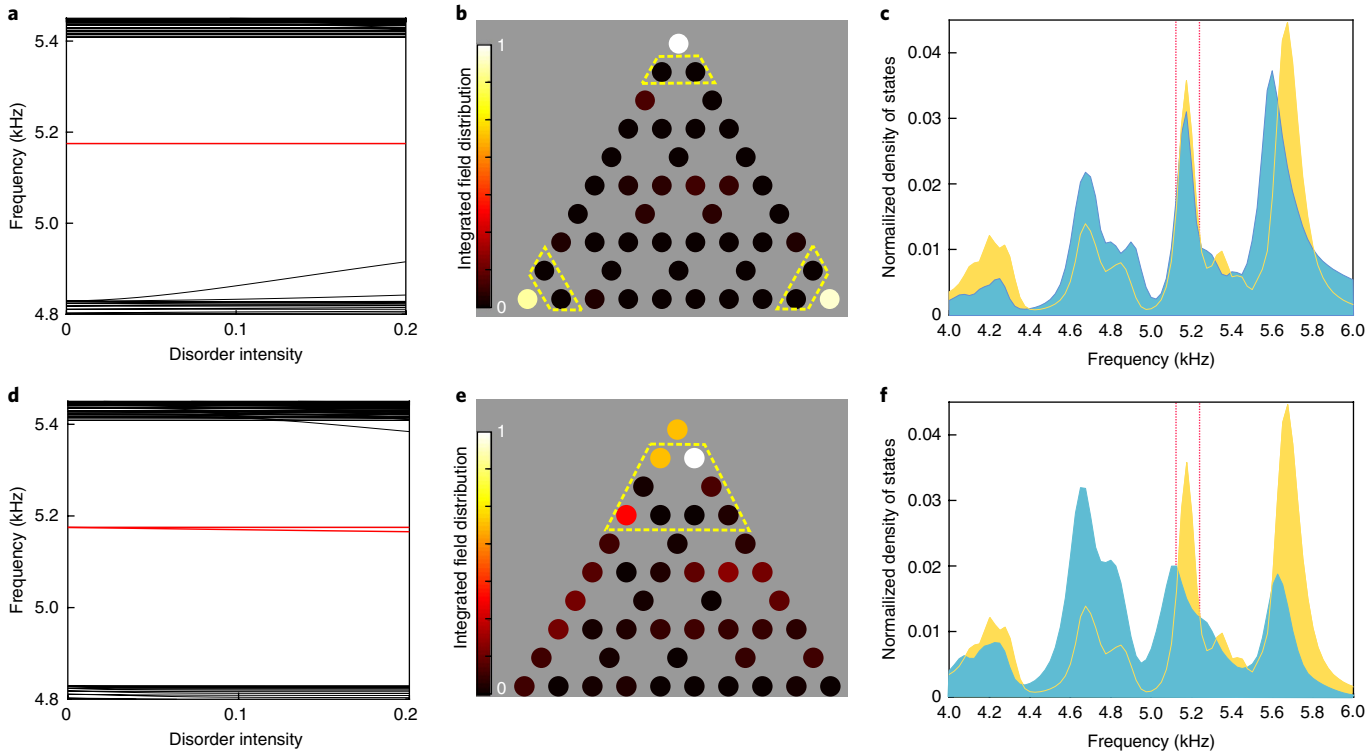

Fig. 3 | Effect of disorder and robustness of the corner states. a,**d**, TBM results demonstrating the pinned (**a**) and deviated (**d**) character of the corner state in the presence of disorder inside yellow dashed regions in **b** and **e**, respectively. Triangular kagome lattice consisting of 20 trimers at each site, disordered sites are perturbed by small deviations in their height, and the disorder parameters are randomly generated. The disorder intensity represents the ratio of the deviation over the unperturbed height. **b**,**e**, Field distribution integrated over the frequency range of corner states. **c**,**f**, Normalized density of states for the lattice in **b** and **e**, respectively, marked by the blue shaded curve, and the density of states for the non-disordered lattice also plotted in as the yellow shaded curve for comparison. The red dashed lines indicate the range of the corner spectrum. The specific disorder parameters can be found in the section 'Disorder parameters' in Methods.

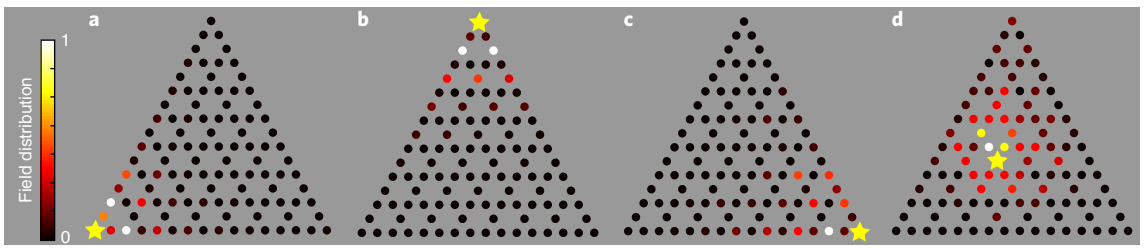

Fig. 4 | Experimental demonstration of corner states coexisting with continuum of bulk modes. a–**d**, Field distribution in the lattice caused by the source located (as indicated by the yellow star) at the bottom left corner (**a**), top corner (**b**), bottom right corner (**c**), or in the bulk (**d**). The excitation frequency is ~5,250 Hz. Due to the narrower topological bandgap and weaker localization of the corner states, the size of the fabricated structure was increased to eight trimers for each edge.

distributed over the central region of the lattice, leading to negligible coupling with the source at the corner sites. Results shown in Fig. 4a–c prove that the corner states remain localized to the corners and do not radiate into the bulk. At the same time, the source, at the same frequency, excited predominantly bulk states when placed inside the structure. Only one corner state was excited weakly in this case, due to some spatial overlap of the pressure field produced by the source with that of the exponentially localized corner states. These results show that, despite their spectral overlap and momentum compatibility, the discrete corner states remain embedded in the bulk continuum without coupling to it, opening a door for studying ultrasharp Fano resonances with topological discrete states, when coupling with the continuum is controllably introduced by deliberate symmetry reduction. It is interesting that the confinement of the corner state to the sublattice allows us to predict which of the three corner states will lift up due to the bulk excitation. For the case of Fig. 4d, the bulk excitation is in the upper site of a trimer in the central bulk, which ensures that the corner state at the upper corner will be excited. This indeed can be seen from the field distribution in Fig. 4d.

Discussion

The topological states induced by bulk polarization introduced in this paper, as well as in the recent work[59], have great potential for applications over a broad range of disciplines, from photonics to acoustics and mechanical vibrations. We have shown that the synthetic degrees of freedom enabled by tuning the neighbour hopping in the crystalline lattice can be beneficial for generating nontrivial bulk polarization states, for the design of systems supporting unconventional edge and corner states. Unique features, such as pinning to 'zero energy', robustness and the non-radiative character of higher-order topological embedded eigenstates significantly expand our ability to control, trap, and steer waves, enabling a plethora of applications, from robust tunable waveguides to a generation of high-fidelity topological sensors. We believe that our work opens important directions in acoustics and beyond, offering possibilities to control waves in unprecedented ways.

Online content

Any methods, additional references, Nature Research reporting summaries, source data, statements of data availability and associated accession codes are available at https://doi.org/10.1038/s41563-018-0252-9.

Received: 31 July 2018; Accepted: 14 November 2018;
Published online: 31 December 2018

References

1. Haldane, F. D. M. Model for a quantum Hall effect without Landau levels: Condensed-matter realization of the 'parity anomaly'. *Phys. Rev. Lett.* **61**, 2015–2018 (1988).
2. Kane, C. L. & Mele, E. J. Quantum spin Hall effect in graphene. *Phys. Rev. Lett.* **95**, 226801 (2005).
3. Kane, C. L. & Mele, E. J. Z_2 topological order and the quantum spin Hall effect. *Phys. Rev. Lett.* **95**, 146802 (2005).
4. Xiao, D., Yao, W. & Niu, Q. Valley-contrasting physics in graphene: Magnetic moment and topological transport. *Phys. Rev. Lett.* **99**, 236809 (2007).
5. Hasan, M. Z. & Kane, C. L. Colloquium: Topological insulators. *Rev. Mod. Phys.* **82**, 3045–3067 (2010).
6. Qi, X. L. & Zhang, S. C. Topological insulators and superconductors. *Rev. Mod. Phys.* **83**, 1057–1110 (2011).
7. Bernevig, B. A. & Hughes, T. L. *Topological Insulators and Topological Superconductors* (Princeton Univ. Press, Princeton, 2013).
8. Haldane, F. D. M. & Raghu, S. Possible realization of directional optical waveguides in photonic crystals with broken time-reversal symmetry. *Phys. Rev. Lett.* **100**, 013904 (2008).
9. Raghu, S. & Haldane, F. D. M. Analogs of quantum-Hall-effect edge states in photonic crystals. *Phys. Rev. A* **78**, 033834 (2008).
10. Wang, Z., Chong, Y. D., Joannopoulos, J. D. & Soljacic, M. Observation of unidirectional backscattering-immune topological electromagnetic states. *Nature* **461**, 772–775 (2009).
11. Feng, L. et al. Nonreciprocal light propagation in a silicon photonic circuit. *Science* **333**, 729–733 (2011).
12. Hafezi, M., Demler, E. A., Lukin, M. D. & Taylor, J. M. Robust optical delay lines with topological protection. *Nat. Phys.* **7**, 907–912 (2011).
13. Fang, K. J., Yu, Z. F. & Fan, S. H. Realizing effective magnetic field for photons by controlling the phase of dynamic modulation. *Nat. Photon.* **6**, 782–787 (2012).
14. Fang, K. J. & Fan, S. H. Controlling the flow of light using the inhomogeneous effective gauge field that emerges from dynamic modulation. *Phys. Rev. Lett.* **111**, 203901 (2013).
15. Khanikaev, A. B. et al. Photonic topological insulators. *Nat. Mater.* **12**, 233–239 (2013).
16. Rechtsman, M. C. et al. Photonic Floquet topological insulators. *Nature* **496**, 196–200 (2013).
17. Lu, L., Joannopoulos, J. D. & Soljaclc, M. Topological photonics. *Nat. Photon.* **8**, 821–829 (2014).
18. Plotnik, Y. et al. Observation of unconventional edge states in 'photonic graphene'. *Nat. Mater.* **13**, 57–62 (2014).
19. Skirlo, S. A., Lu, L. & Soljacic, M. Multimode one-way waveguides of large Chern numbers. *Phys. Rev. Lett.* **113**, 113904 (2014).
20. Skirlo, S. A. et al. Experimental observation of large Chern numbers in photonic crystals. *Phys. Rev. Lett.* **115**, 253901 (2015).
21. Wu, L. H. & Hu, X. Scheme for achieving a topological photonic crystal by using dielectric material. *Phys. Rev. Lett.* **114**, 223901 (2015).
22. Cheng, X. J. et al. Robust reconfigurable electromagnetic pathways within a photonic topological insulator. *Nat. Mater.* **15**, 542–548 (2016).
23. Leykam, D., Rechtsman, M. C. & Chong, Y. D. Anomalous topological phases and unpaired Dirac cones in photonic Floquet topological insulators. *Phys. Rev. Lett.* **117**, 013902 (2016).
24. Khanikaev, A. B. & Shvets, G. Two-dimensional topological photonics. *Nat. Photon.* **11**, 763–773 (2017).
25. Ozawa, T. et al. Topological photonics. Preprint at https://arXiv.org/abs/1802.04173v1 (2018).
26. Peano, V., Brendel, C., Schmidt, M. & Marquardt, F. Topological phases of sound and light. *Phys. Rev. X* **5**, 031011 (2015).
27. Yang, Z. J. et al. Topological acoustics. *Phys. Rev. Lett.* **114**, 114301 (2015).
28. Huber, S. D. Topological mechanics. *Nat. Phys.* **12**, 621–623 (2016).
29. Susstrunk, R. & Huber, S. D. Classification of topological phonons in linear mechanical metamaterials. *Proc. Natl Acad. Sci. USA* **113**, E4767–E4775 (2016).
30. Xiao, M. et al. Geometric phase and band inversion in periodic acoustic systems. *Nat. Phys.* **11**, 240–244 (2015).
31. Kitaev, A. Yu. Unpaired Majorana fermions in quantum wires. *Phys.-Uspekhi* **44**, 131 (2001).
32. Barik, S. et al. A topological quantum optics interface. *Science* **359**, 666–668 (2018).
33. Bahari, B. et al. Nonreciprocal lasing in topological cavities of arbitrary geometries. *Science* **358**, 636–639 (2017).
34. Bandres, M. A. et al. Topological insulator laser: Experiments. *Science* **359**, eear4005 (2018).
35. Harari, G. et al. Topological insulator laser: Theory. *Science* **359**, eear4003 (2018).
36. Ni, X. et al. Spin- and valley-polarized one-way Klein tunneling in photonic topological insulators. *Sci. Adv.* **4**, eeap8802 (2018).
37. Fang, C., Gilbert, M. J. & Bernevig, B. A. Bulk topological invariants in noninteracting point group symmetric insulators. *Phys. Rev. B* **86**, 115112 (2012).
38. Benalcazar, W. A., Bernevig, B. A. & Hughes, T. L. Quantized electric multipole insulators. *Science* **357**, 61–66 (2017).
39. Benalcazar, W. A., Bernevig, B. A. & Hughes, T. L. Electric multipole moments, topological multipole moment pumping, and chiral hinge states in crystalline insulators. *Phys. Rev. B* **96**, 245115 (2017).
40. Serra-Garcia, M. et al. Observation of a phononic quadrupole topological insulator. *Nature* **555**, 342–345 (2018).
41. Peterson, C. W., Benalcazar, W. A., Hughes, T. L. & Bahl, G. A quantized microwave quadrupole insulator with topologically protected corner states. *Nature* **555**, 346–350 (2018).
42. Imhof, S. et al. Topolectrical circuit realization of topological corner modes. *Nat. Phys.* **14**, 925–929 (2018).
43. Langbehn, J., Peng, Y., Trifunovic, L., von Oppen, F. & Brouwer, P. W. Reflection-symmetric second-order topological insulators and superconductors. *Phys. Rev. Lett.* **119**, 246401 (2017).
44. Ezawa, M. Higher-order topological insulators and semimetals on the breathing kagome and pyrochlore lattices. *Phys. Rev. Lett.* **120**, 026801 (2018).
45. Geier, M., Trifunovic, L., Hoskam, M. & Brouwer, P. W. Second-order topological insulators and superconductors with an order-two crystalline symmetry. *Phys. Rev. B* **97**, 205135 (2018).
46. Ezawa, M. Minimal models for Wannier-type higher-order topological insulators and phosphorene. *Phys. Rev. B* **98**, 045125 (2018).
47. Khalaf, E. Higher-order topological insulators and superconductors protected by inversion symmetry. *Phys. Rev. B* **97**, 205136 (2018).
48. Kunst, F. K., van Miert, G. & Bergholtz, E. J. Lattice models with exactly solvable topological hinge and corner states. *Phys. Rev. B* **97**, 241405(R) (2018).
49. Ezawa, M. Strong and weak second-order topological insulators with hexagonal symmetry and Z_3 index. *Phys. Rev. B* **97**, 241402(R) (2018).
50. Song, Z. D., Fang, Z. & Fang, C. (d−2)-dimensional edge states of rotation symmetry protected topological states. *Phys. Rev. Lett.* **119**, 246402 (2017).
51. Schindler, F. et al. Higher-order topological insulators. *Sci. Adv.* **4**, eaat0346 (2018).
52. Ni, X., Gorlach, M. A., Alù, A. & Khanikaev, A. B. Topological edge states in acoustic kagome lattices. *New J. Phys.* **19**, 055002 (2017).
53. Noh, J. et al. Topological protection of photonic mid-gap defect modes. *Nat. Photon.* **12**, 408–415 (2018).
54. Marinica, D. C., Borisov, A. G. & Shabanov, S. V. Bound states in the continuum in photonics. *Phys. Rev. Lett.* **100**, 183902 (2008).
55. Hsu, C. W. et al. Observation of trapped light within the radiation continuum. *Nature* **499**, 188–191 (2013).
56. Zhen, B., Hsu, C. W., Lu, L., Stone, A. D. & Soljacic, M. Topological nature of optical bound states in the continuum. *Phys. Rev. Lett.* **113**, 257401 (2014).

57. Hsu, C. W., Zhen, B., Stone, A. D., Joannopoulos, J. D. & Soljacic, M. Bound states in the continuum. *Nat. Rev. Mater.* **1**, 16048 (2016).
58. Doeleman, H. M., Monticone, F., den Hollander, W., Alù, A. & Koenderink, A. F. Experimental observation of a polarization vortex at an optical bound state in the continuum. *Nat. Photon.* **12**, 397–401(2018).
59. Xue, H., Yang, Y., Gao, F., Chong, Y. D. & Zhang, B. Acoustic higher-order topological insulator on a kagome lattice. *Nat. Mater.* https://doi.org/10.1038/s41563-018-0251-x (2018).

Acknowledgements

The work was supported by the Defense Advanced Research Projects Agency under the Nascent programme with grant number HR00111820040, and by the National Science Foundation with grant numbers CMMI-1537294, EFRI-1641069 and DMR-1809915. Research was carried out in part at the Center for Functional Nanomaterials, Brookhaven National Laboratory, which is supported by the US Department of Energy, Office of Basic Energy Sciences, under contract number DE-SC0012704.

Author contributions

All authors contributed extensively to the work presented in this paper.

Competing interests

The authors declare no competing interests.

Additional information

Supplementary information is available for this paper at https://doi.org/10.1038/s41563-018-0252-9.

Reprints and permissions information is available at www.nature.com/reprints.

Correspondence and requests for materials should be addressed to A.A. or A.B.K.

Publisher's note: Springer Nature remains neutral with regard to jurisdictional claims in published maps and institutional affiliations.

Methods

Structure design, 3D printing, and generic measurements. The unit cell designs of the topological lattice and trivial lattice are plotted in Fig. 1b, c, where the lattice constant of the structure is $a_0 = 39.75$ m*m*, and the height of cylinder is chosen as $H_0 = 40.52$ m*m*, with the radius $R_0 = 5.77$ mm, such that the frequencies of the desired mode are in the probing range of the microphone. The connectors between the cylinders consist of blocks, with their dimensional sizes $L_a = 8.34$ m*m*, $L_b = 7.95$ m*m* and $L_c = 2.64$ m*m*, respectively. The coupling strength of the modes is maximal when the connectors are at the top or bottom of the cylinders, and minimum at the centre of the cylinders. To make the intra-cell and inter-cell coupling of the trimers inequivalent, the outer connectors of the topological trimer shown in Fig. 1b are placed at the top and bottom of the cylinders, while the inner connectors are shifted towards the centre by a distance $H_a = 10.23$ m*m*. The trivial trimer, in Fig. 1c, is the opposite way around. The boundary cells, shown in the photograph of the fabricated structure (Fig. 1h), have the same parameters as the trimers, except their heights are half the trimers' height.

The trimers and boundary cells were fabricated using a B9Creator v1.2 3D printer. All cells were made with acrylic-based light-activated resin, a type of plastic that hardens when exposed to ultraviolet light. Each cell was printed with a sufficient thickness to ensure a hard wall boundary condition and narrow probe channels were intentionally introduced on the top and bottom sides of each of the cylinders to excite and measure the local pressure field at each site. The diameter of the port is $D_0 = 3.73$ mm, and the upper port has a height $H_d = 3.97$ mm, while the height of lower port is $2H_d$. When not in use, the probe channels were closed with 3D-printed cups. The trimers and boundary cells were printed one at a time and the models were designed specifically to interlock tightly with each other. The non-trivial and trivial structures shown in Fig. 1 both consist of 15 trimers and 18 boundary cells. For the studying lattice corner states in the continuum in Fig. 4, 36 trimers and 27 boundary cells are used. For all measurements, a frequency generator and FFT spectrum analyser scripted in LabVIEW were used. The FFT spectrum analyser is also capable of extracting phase differences between two channels.

Numerical methods. The finite element solver Multiphysics Comsol 5.2a and the acoustic module were used to perform full-wave simulation. In the acoustic propagation wave equation, the speed of sound was set as 343.2 m s^{-1} and density of air as 1.225 kg m^{-3}. Other dimensional parameters of the structure are the same as the fabricated parameters. For bulk (edge) band structure calculations, periodic boundary conditions were imposed along the edges of the unit cell (supercell). Large-scale simulations were performed with hard-wall boundary conditions applied on the boundary cells. To extract the bulk polarization from simulation results, we took the average value of the acoustic pressure field on the top or bottom of the cylinders for the mode of interest (lowest frequency bulk mode for bulk polarization and lower edge mode for edge polarization); the acoustic pressure field was used to construct the eigenstates of the mode, and we evaluated the phase ϕ_{C_3} based on the normalized eigenstates.

The TBM is used to fit the band diagram of the topological and trivial structures and also to verify the correctness of ϕ_{C_3} graph based on the eigenstates calculation. For the gapless band diagram, the onsite frequency is fitted as $\omega_0 = 5,182.5$ Hz, and the coupling strength as $\kappa = \gamma = -310$ Hz. For the topological band diagram, these fitted parameters are $\omega_0 = 5,133$ Hz, $\kappa = 115.5$ Hz and $\gamma = 462$ Hz and for trivial band diagram, the onsite frequency is the same as the topological band diagram with the magnitudes of κ and γ flipped. For the acoustic spectra, the fitted onsite energy $\omega_0 = 5,175$ Hz and the other parameters are the same as the ones in the band diagram.

Phase difference measurement. A set of two compact magnetic transducers was used to excite local pressure fields and two directional microphones (Model:EMM-6) were connected to an external two-port digital data acquisition device (AUBIO BOX USB 96), enabling excitation of the desirable phase profiles and measurements of the phase across the structure. For the phase differences, all the upper ports were open to allow the modes to propagate with vast loss, thus minimizing the wave reflection at the boundary. The speaker was placed at the site in the centre of the structure, and two microphones were placed at the two sites within a bulk trimer near to the speaker, as shown in Fig. 1h. The frequency generator was used to run a sweep of monochromatic frequencies from 4,000 Hz to 4,550 Hz in 25 Hz intervals, with a dwell time of 4 s (to allow for stability of the profile) and determine the phase differences between the two channels at each frequency; for example, the phase difference between site 1 and site 2 was measured as φ_{12}. One of the microphones was also switched to the third site (from site 2 to site 3) in the same trimer to measure the second phase difference φ_{13}. Since the detected modes near the source behave like bulk modes of the infinite structure because of the loss in the system and its relatively large size (when all upper and lower ports—the probe holes—are open and leak), it is legitimate to construct the normalized eigenvectors of the bulk modes by these measured phase differences as $1/\sqrt{3}\,(1, e^{i\varphi_{12}}, e^{i\varphi_{13}})$. Finally, with the information about the eigenvectors, the phase ϕ_{C_3} is extracted, as shown by Fig. 1i.

Density of states measurement. The speaker was placed at the bottom port and the microphone at the top port of the same site. A tiny gap was left between the speaker and the port to allow for the presence of reflection channels, while the microphone was touched closely to the port to achieve the maximum absorption. The frequency generator was used to run a sweep from 3,600 Hz to 6,000 Hz in 25 Hz intervals with a dwell time of 4 s while the FFT spectrum analyser obtained the amplitude responses $\varphi(\omega)$ at each frequency. Field distributions $\varphi(i,\omega)$ are obtained by repeating this process for each site i. Since it is difficult to guarantee the tiny gap is exactly the same for every site, and the amplitude response is highly sensitive to this tiny gap, we normalized the data for each site based on the total spectra summed over frequencies as well as on the free-space amplitude response between the microphone and the speaker, $\Phi(i,\omega) = \varphi(i,\omega)/\sum_\omega \varphi(i,\omega)/\varphi_{\text{air}}(\omega)$. After that, we squared the signal $\Phi_n(i,\omega)$ and averaged the power spectrum for an array of N resonators $P_a(\omega) = \sum_i |\Phi(i,\omega)|^2/N$ to get the normalized spectra, $P_n(\omega) = P_a(\omega)/\sum_\omega P_a(\omega)$, the equivalent to the density of states of the kagome lattice. For the field profiles excited by a single frequency, the speaker was fixed at the port of the site of interest and the microphone was placed over each site of the lattice to measure the magnitude response at the desired frequency (for example, 5,250 Hz for the corner state in Fig. 4).

Disorder parameter. In the first disorder configuration shown in Fig. 4a, the disorder parameters are generated by the random function in a MATLAB script, and converted to small deviations of the height H_0; the ratios of the perturbed height over H_0 were 1.00, 0.9076, 1.05, 0.9607, 0.9820, 1.0340, 0.9961, 0.9220, 1.0182. In the second disorder configuration in Fig. 4b, the disorder parameters are 1.00, 0.9076, 1.05; 1.00, 0.9744, 1.0273, 1.00, 0.9348, 1.043.

Data availability

Data that are not already included in the paper and/or in the Supplementary Information are available on request from the authors.